ARL-TR-8961 • May 2020

Microstructure-Based Model of the Deformation and Failure Response of the Human Skull under Uniaxial Compression

by Stephen Alexander and Tusit Weerasooriya

NOTICES

Disclaimers

ARL-TR-8961 ● MAY 2020

Microstructure-Based Model of the Deformation and Failure Response of the Human Skull under Uniaxial Compression

Stephen Alexander
SURVICE Engineering Company

Tusit Weerasooriya
Weapons and Materials Research Directorate, CCDC Army Research Laboratory

REPORT DOCUMENTATION PAGE	*Form Approved* *OMB No. 0704-0188*

1. REPORT DATE *(DD-MM-YYYY)*	2. REPORT TYPE	3. DATES COVERED (From - To)
May 2020	Technical Report	1 October 2018–30 September 2019

4. TITLE AND SUBTITLE
Microstructure-Based Model of the Deformation and Failure Response of the Human Skull under Uniaxial Compression

5a. CONTRACT NUMBER
W911QX-16-D-0014

5b. GRANT NUMBER

5c. PROGRAM ELEMENT NUMBER

6. AUTHOR(S)
Stephen Alexander and Tusit Weerasooriya

5d. PROJECT NUMBER

5e. TASK NUMBER

5f. WORK UNIT NUMBER

7. PERFORMING ORGANIZATION NAME(S) AND ADDRESS(ES)
CCDC Army Research Laboratory*
ATTN: FCDD-RLW-PB
Aberdeen Proving Ground, MD 21005

8. PERFORMING ORGANIZATION REPORT NUMBER
ARL-TR-8961

9. SPONSORING/MONITORING AGENCY NAME(S) AND ADDRESS(ES)

10. SPONSOR/MONITOR'S ACRONYM(S)

11. SPONSOR/MONITOR'S REPORT NUMBER(S)

12. DISTRIBUTION/AVAILABILITY STATEMENT
Approved for public release; distribution is unlimited.

13. SUPPLEMENTARY NOTES
ORCID ID: Tusit Weerasooriya, 0000-0003-3299-2166
*As of 31 January 2019, the Army Research Laboratory is part of the US Army Combat Capabilities Development Command (CCDC) (formerly RDECOM) and is now called CCDC Army Research Laboratory.

14. ABSTRACT
Numerical studies for head injury from applied loading can be made more biofidelic by incorporating mechanism-based, microstructurally inspired material models representing the mechanical response and fracture of the human skull. A hybrid experimental–modeling computational (HEMC) concept was used to develop a mesoscale finite-element (FE) model of the heterogeneous microstructure of a human skull coupon. Elements were mapped to corresponding regions from micro-computed tomography images, and the bone volume fraction (BVF) of each element was identified. Then, element-specific moduli were calculated from a BVF–modulus power relationship previously derived from experiments with critical assumptions. The simulation was able to match within 5% of the measured global modulus, thus validating the use of assumptions in the derivation of initial linear response. The subsequent nonlinear response, up to the point of instability from pore collapse, was represented by failure of elements either by compression or tension. Evolution of measured nonuniform full-strain fields on coupon surfaces, showing localized regions of failure, was compared between experiment and simulation and was qualitatively similar, thus validating the HEMC procedure with failure concepts. The methodology enabled identification of failure locations within the skull coupon, thereby providing a tool to predict localized failure initiation in FE simulations at larger length scales.

15. SUBJECT TERMS
skull fracture, skull finite-element simulation, skull mechanics, head simulation, micro-computed tomography, CT

16. SECURITY CLASSIFICATION OF:			17. LIMITATION OF ABSTRACT	18. NUMBER OF PAGES	19a. NAME OF RESPONSIBLE PERSON
					Stephen Alexander
a. REPORT	b. ABSTRACT	c. THIS PAGE			19b. TELEPHONE NUMBER (Include area code)
Unclassified	Unclassified	Unclassified	UU	53	(410) 306-0917

Standard Form 298 (Rev. 8/98)
Prescribed by ANSI Std. Z39.18

Contents

List of Figures

Acknowledgments

The authors express deep appreciation for the gracious help provided by Dr Richard Becker of the US Army Combat Capabilities Development Command Army Research Laboratory. He generously spent time helping to overcome difficulties encountered with Abaqus. Specifically, his suggestions to try to model the response of failed elements with a pressure–volume relationship proved invaluable, enabling the simulation to continue after local failure up to the initiation of global catastrophic failure.

1. Introduction

Numerical models of the head and the upper body are used to design and evaluate head protection against various externally applied loading to the head. A key component to the reliability of these models is the accuracy with which the deformation and final failure (fracture) response and associated failure mechanisms of the skull—the natural protection of the brain—are represented. The skull is heterogeneous due to its sandwich structure, with dense outer and inner layers (tables) surrounding a highly porous inner layer (the diploe). The porosity changes substantially as a function of thickness, from averages of 7% at the outer table, rising to 58% in the diploe, and reducing to 16% in the inner table on average (Alexander et al. 2019c). Furthermore, the porosity can peak to more than 80% in the diploe.

Bone volume fraction (BVF), which is the porosity percentage subtracted from 100%, is commonly related to the modulus and strength of porous bone by a power relationship, as reviewed by Helgason et al. (2008) and Morgan et al. (2018). Musy/Maquer et al. (2017) demonstrated that compared with other morphological parameters, BVF, the higher-scale microstructural measure, is the single best predictor of both the stiffness and yield strength of trabecular bone for a specific age of a species (thus the same bone chemistry). Motivated by the mechanical implications of the BVF on the microstructure, researchers at the US Army Combat Capabilities Development Command (CCDC) Army Research Laboratory (ARL) recently proposed and optimized a power relationship between the BVF and the modulus (E) for the human skull bone based on compression experiments using multiple fresh-frozen and thawed human skull bone coupons (Alexander et al. 2020). Modulus values at a given normalized depth for the human skull were calculated from the power relationship for use in finite-element (FE) simulations at three different scales: a single modulus for the entire thickness of the skull, moduli for each of the three layers of the sandwich structure (outer table, mid-diploe, and inner table), and a continuous representation along the normalized depth.

However, the parameters of the skull-bone power relationship were derived from experimental measurements on multiple specimens with two critical assumptions. These assumptions were based on considering the full skull structure as a series of stacked layers, each layer having its own uniform properties, for purposes of developing the analytical power-law model based on the possible experimental measurements. The first assumption was that the strain within each layer was uniform and equal to the average *surface strain* of each layer, measured using digital image correlation (DIC). The second assumption was that stress measured at the load cell was assumed to be the uniaxial compressive stress acting throughout the structure, and hence on each layer. These assumptions were motivated in part from earlier experiments on minipig skulls, which showed that the *surface strain* formed a gradient of layers along the compression direction that was normal to the outer surface of the skull (Alexander et al. 2019a). However, the use of these assumptions remained to be validated in the heterogeneous human skull using rigorous 3-D analysis coupled with the evolution of the measured global stress–strain and full-field localized nonuniform surface strains up to failure.

The purpose of the present detailed study was to verify the assumptions used as the starting point for the development of the analytical relationship between BVF and modulus as well as to develop mechanism-based microstructurally inspired failure models for skull bone at coupon specimen scale. This was accomplished with a detailed 3-D FE simulation of one of the compression experiments from the multiple specimens used to derive the CCDC Army Research Laboratory human-skull power relationship. The most-basic means of testing these assumptions would be to simulate the experiment with an FE mesh replicating the complete intricate details of the 3-D structure of the bone. Such a mesh would be created by converting high-resolution micro-computed tomography (micro-CT) scans of the skull bone into volumetric meshes through a labor-intensive process that would require a prohibitively large number of elements due to the complex 3-D shape of the bone and porous features. Therefore, in this report, to verify the human skull E–BVF power relationship derived with the critical assumptions and also to inversely derive failure laws rather than attempting to mesh the bone structure in detail, a simpler method was used to fill the space with elements and map them to the corresponding mesostructural elements from the measured micro-CT data. For each element, the BVF of the physical volume the element represented could be calculated. Then, element-specific mechanical properties could be calculated based on the BVF of the element. An in-house method for mapping the elements to the micro-CT data has been previously developed (Alexander et al. 2019b) and will be used in the present report due to the ease of its implementation.

However, the power relationship described only the initial linear response of the human skull bone, whereas skull coupons compressed experimentally show a distinct three-part apparent nonlinear global response, which also included trabecular collapse and densification (Robbins and Wood 1969; Boruah et al. 2013; Alexander et al. 2020). For instance, Fig. 1 provides an example from the literature of the three-part global response. The transition point between the first and second parts corresponded to the start of the discontinuous diploe failure and was identified by a local maximum in the load-displacement response. The transition is referred to here as the start of the instability, as marked in Fig. 1. When further analyzed the first part of the response was found to consist of two distinct subregimes: an initial linear elastic regime followed by a nonlinear regime leading to the instability point (Fig. 1 inset). Deviation from the initial linear elastic response could most probably be due to initiation of localized failure in some regions within the specimen. Based on this hypothesis, in the present study it was assumed that some of the elements failed during the loading in this regime. The nonlinear response of bone samples observed experimentally at the macro scale has likewise been previously simulated by implementing nonlinear material properties on an element-by-element basis. For example, Hambli (2013) used a micro-level mesh of only the bone phase of trabecular bone structures such that elements had an average size of 20 μm and were represented only with dense bone material (BVF = 1). Critical strain thresholds were set for compression and tension, and when elements exceeded these thresholds their stiffness was reduced. In simulating the femur, both Bessho et al. (2007) and Ariza et al. (2015) used much larger elements (3 mm), which represented a mixture of bone and marrow. Each element was assigned a nonlinear material response that included postyield softening and was dependent on the BVF of the element. Bessho et al. (2007) also included failure criteria such that elements that met these threshold conditions were subsequently considered nonloadbearing.

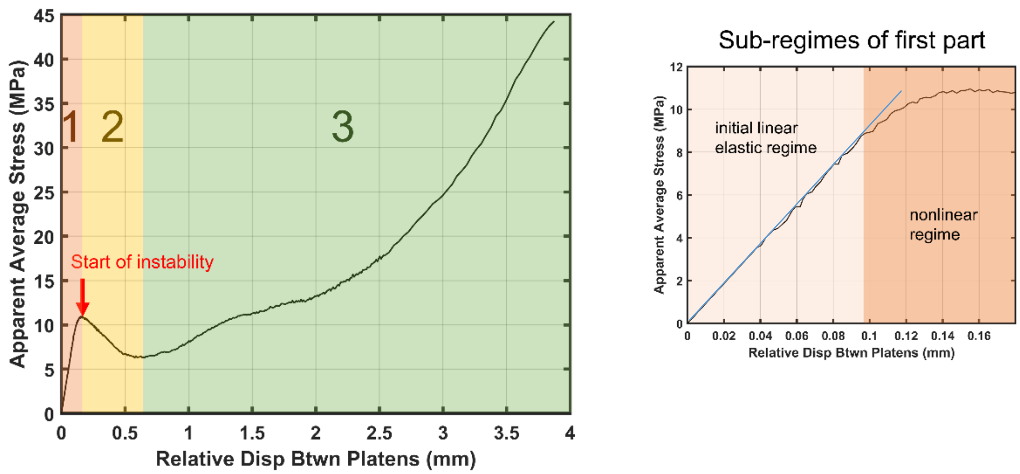

Fig. 1 **(left) Example of the three-part global nonlinear response of human skull coupons loaded in compression (modified from Alexander et al. 2020). The transition between the first and second parts represents the start of the instability. (right) Subset shows the two subregimes within the first part: an initial linear elastic regime followed by a nonlinear regime leading to the start of the instability.**

The first part of the present study validates the use of the critical assumptions, based on the representation by a stacked uniform layered structure, to derive the initial linear elastic power-law representation of the response. In the second part, the experimentally measured subsequent nonlinear response prior to the start of the instability (Fig. 1) was simulated by modeling failure at the element level. Critical tensile- and compressive-failure stress thresholds were identified through an iterative process. These stress thresholds were assumed to be dependent on the BVF by power relationships, similar to the E–BVF relationship, and several iterations of simulations were needed to identify suitable parameter values. The principal stress components of the element were monitored, and when these exceeded the failure thresholds, the element was considered to have failed.

2. Methods

2.1 Specimen Extraction and Compression

The skull specimen measured approximately 8 × 8 mm on the outer surface and included the entire thickness of the skull from the inner to outer surfaces. After extraction the specimen was imaged with high-resolution micro-CT (5.3 µm). Details of extraction and micro-CT imaging have been previously documented in which the specimen of the current report was labeled and referred to as Specimen 04-09 (Alexander et al. 2019c). The specimen was then quasi-statically compressed as previously documented (Alexander et al. 2020, with additional information in Alexander et al. 2018). The experiment was conducted in compliance with ARL's Policy for Use of Human Cadavers for Research, Development, Test, and Evaluation under the guidance and oversight of the ARL Human Cadaver Review Board and the ARL Safety Office. Briefly, the specimen was loaded in the through-thickness dimension. The outer and inner surfaces of the skull coupon were each in contact with compression platens. These outer and inner surfaces are hereafter referred to as the top and bottom of the specimen, respectively. Likewise, the compression platen in contact with the top surface is referred to as the top platen, and the platen in contact with the bottom surface is referred to as the bottom platen. The specimen was compressed by displacing one of the compression platens in the through-thickness dimension at a constant rate, while the other platen remained stationary. Two of the free nonloaded adjacent faces of the specimen were speckled for tracking full-field displacement and strain using DIC. The speckle patterns of these two faces were imaged during the compression experiment by two separate cameras. The two cameras are hereafter referred to as the left and right cameras, and the two faces of the specimen imaged are referred to as the left and right faces.

The compressive load-displacement response of the specimen showed three different phases, as reported in the previous publication of Alexander et al. (2020). Here, only the initial phase, up to the start of instability (defined in Fig. 1), was modeled. Figure 2 shows this portion of experimentally measured apparent stress as a function of the compressive strain for Specimen 04-09. The apparent stress was calculated by normalizing the force recorded by the load cell by the original cross-sectional area of the specimen. The apparent compressive strain in the experiment was calculated by averaging the 2-D strain fields over the two faces of the specimen, which were speckled for DIC.

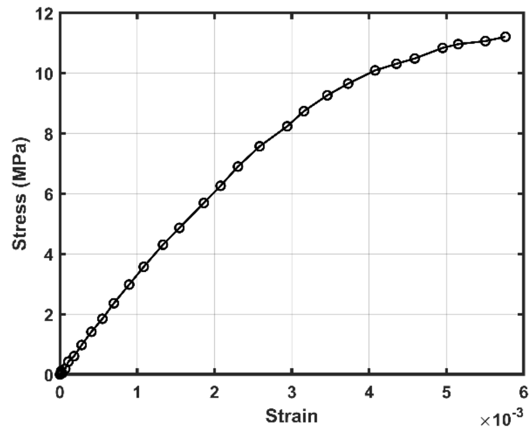

Fig. 2 Apparent stress and strain of Specimen 04-09 measured experimentally during quasi-static compression prior to the start of the instability

2.2 Finite-Element Mesh Generation and Mapping to Micro-CT Images

A volume of interest (VOI) in the form of a rectangular block was selected from the full 3-D shape of the specimen, as shown in Fig. 3. The 3-D space of the rectangular block was then volumetrically meshed with 16,683 tetrahedral elements, ignoring the inner porous structure of the bone. The average element volume was 2.20×10^7 µm^3 ± 1.32×10^7 µm^3.* The original BVF of each element, $f_{BV,0}$, was calculated by mapping the elements to the micro-CT dataset, downsized by a factor of 16 to a resolution of 84.9 µm. The in-house method of calculating $f_{BV,0}$ for each element was previously described (Alexander et al. 2019b). Figure 3 shows the resulting mesh, where the distance between the top and bottom of the mesh, hereafter referred to as the simulated depth, d_{sim}, was less than the distance between the top and bottom of the experimental specimen, d_{exp}.

* The report describing the in-house algorithm for mapping the micro-CT dataset to the FE mesh (Alexander et al. 2019b) reported the volume of the elements incorrectly. The number cited here is correct.

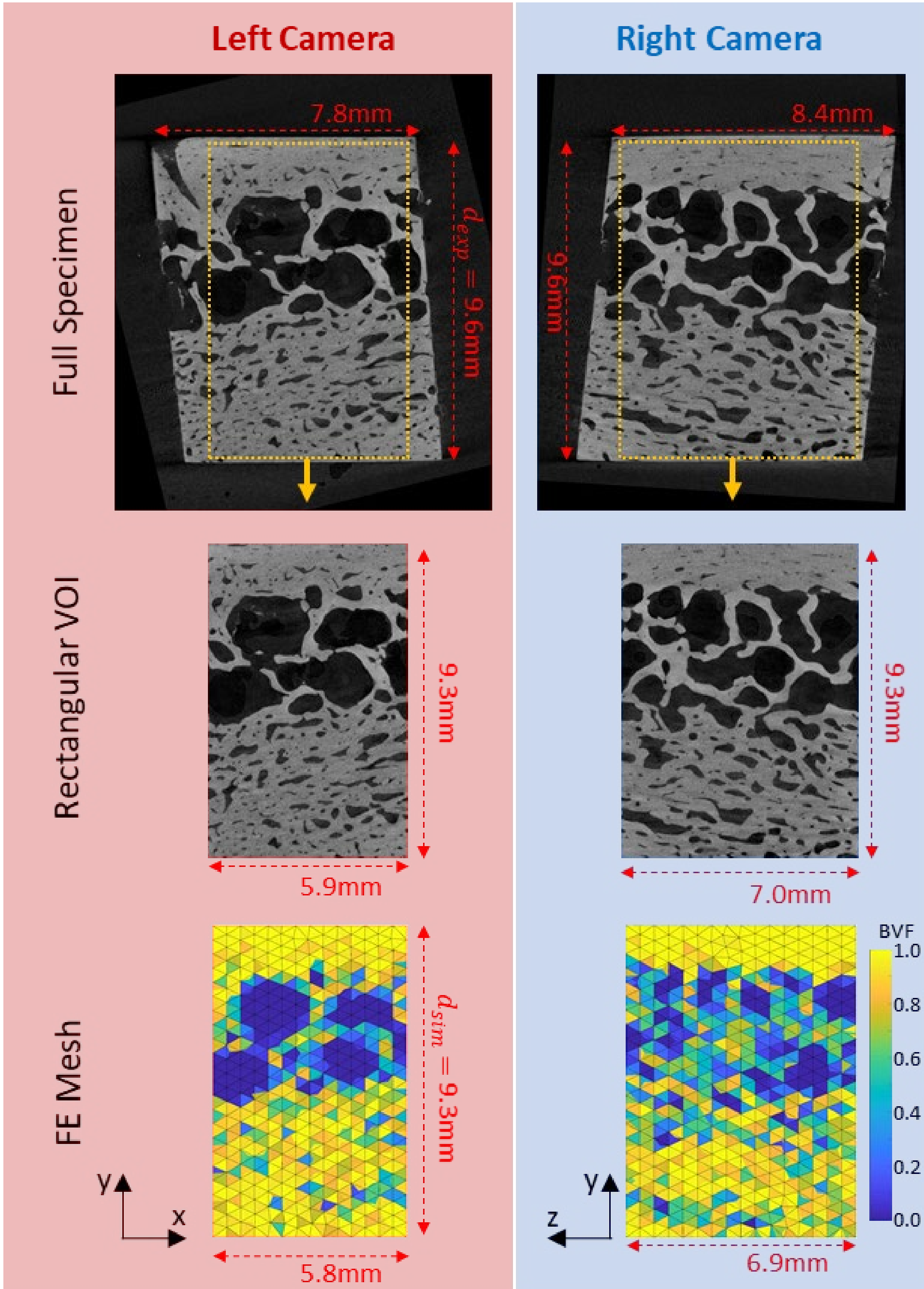

Fig. 3 Comparison of the FE mesh with the morphology of the bone coupon, as imaged using micro-CT. The sides facing the left and right cameras are shown on the left in the red box and on the right in the blue box. Top row shows micro-CT images of the specimen prior to testing. Middle row shows the rectangular-box shaped VOI used for FE meshing. Bottom row shows the FE mesh, with colors corresponding to the original BVF of each element (color bar on right).

The $f_{BV,0}$ value of each element was rounded to the nearest 0.01 to produce a discrete range of 101 different values of BVF, from 0.00 to 1.00. Then the lowest

BVF of 0.00 was artificially assigned a value of 0.001 for the numerical calculations to prevent premature termination of simulations due to highly distorted elements.

Each element was assigned into 1 of 101 different element sets based on $f_{BV,0}$ of the element such that all of the elements within a given element set had the same $f_{BV,0}$ value.

2.3 Simulation of Initial Linear Response

A preliminary simulation modeled only the initial linear response of the experiment, hereafter referred to as the linear simulation. The goal was to check if the modeling framework, with the E–BVF power law applied on an element-by-element basis to the simplified rectangular mesh, could replicate the initial linear modulus from the experiment. The simulation was run in Abaqus Standard 2017, using four processors on Department of Defense High Performance Computing systems. Each of the 101 element sets were assigned unique elastic material properties. The Poisson's ratio was set to 0.3 for all elements. The modulus was calculated based on $f_{BV,0}$ using the previously reported power relationship between modulus, in gigapascals (GPa), and BVF (Alexander et al. 2020):

$$E = 8.528\left(f_{BV,0}\right)^{1.585} \tag{1}$$

The compression described in Section 2.1 was simulated in the following manner. The compression platens located on the top and bottom surfaces of the specimen were modeled as analytical rigid surfaces. The bottom platen was specified to be stationary by constraining all 6 degrees of freedom. The specimen was compressed by displacing the top platen in the through-thickness direction, the y-direction, as depicted in the coordinate system in Fig. 3. The y-direction displacement (v_y) was specified to linearly increase from $v_y = 0$ to $v_y = \delta_{max}^{top}$, where δ_{max}^{top} was the maximum displacement of the top platen. This displacement was chosen to be $\delta_{max}^{top} = 0.03702$ mm. This value was chosen to correspond to an applied strain in the simulation of $\varepsilon_{app} = 0.4\%$, where ε_{app} was the ratio of δ_{max}^{top} to the original depth of the mesh (d_{sim}):

$$\varepsilon_{app} = \delta_{max}^{top}/d_{sim} \tag{2}$$

Contact between the platens and the specimen was modeled using the surface-to-surface contact pair formulation in Abaqus to minimize interpenetration of the surfaces with a penalty method approximation.* A tangential friction coefficient between the specimen and platens was set to $\mu = 0.1$. Preliminary simulations showed that the effect of changing this parameter from $\mu = 0.1$ to $\mu = 0.01$ was negligible (Appendix A).

The stress–strain response of the specimen in the simulation is compared with the experimental response in Fig. 4, where the reported simulated stress was calculated as the resultant force in the compression direction, measured at the top rigid platen, normalized by the original cross-sectional area of the specimen mesh. The reported simulated strain was calculated by normalizing the displacement of the top platen by the original depth of the mesh. For further comparison of the simulation and experiment, Fig. 5 compares the development and localization of loading direction compressive strain in the experiment and simulation. As shown in Figs. 4 and 5, the linear simulation matched the initial linear regime of the experimental response in terms of both modulus and qualitative comparison of the loading direction compressive strain contours.

* Interpenetration of the surfaces was minimized by specifying the pressure–overclosure relationship to be "hard", as defined in the online Abaqus Analysis User's Guide, Section 37.1.2.: Contact Pressure-Overclosure Relationships. This "hard" constraint was enforced via the default method, which for surface-to-surface contact was the penalty method. Constraint enforcement methods are described in the Abaqus Analysis User's Guide, Section 38: Contact Formulations and Numerical Methods.

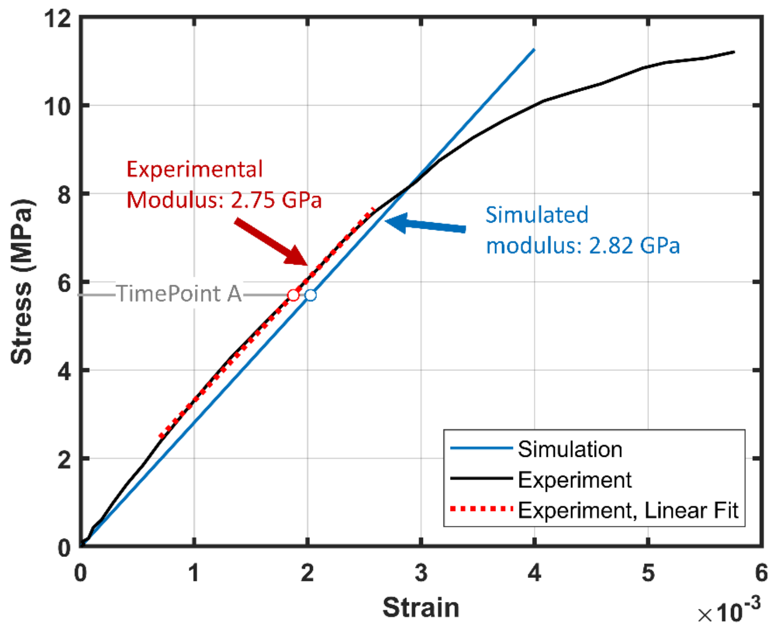

Fig. 4 **Comparison of the apparent stress and strain between the linear simulation and the experiment. The point at which both the simulation and experiment reached an apparent stress level of 5.7 GPa is marked as TimePoint A. This timepoint is used for further analysis of the simulation because it falls within the linear regime of the experimental response, shown as the red dashed line.**

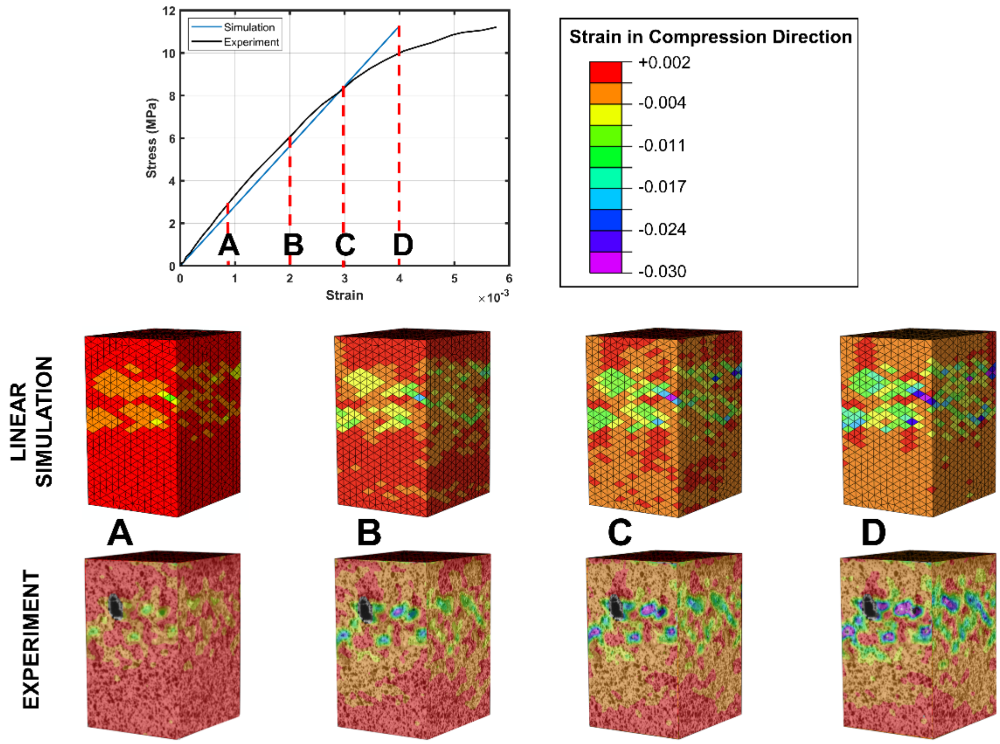

Fig. 5 Strain fields in the loading direction compared between the linear simulation (top row) and experiment (bottom row). Inset at upper right shows color bar for all strain fields. Comparisons are at four different levels of applied strain, labeled A–D and identified on the stress–strain curves at top. At each of the four levels, the sides facing the left and right cameras are shown (identified in Fig. 3). Contours from simulation are plotted on the undeformed mesh.

2.4 Mesoscale Simulation of Failure

To implement the concept of failure in the numerical model, it was assumed that the deviation of the experimental stress–strain relation from linearity is due to failure at the microstructure scale, which can be represented by element failure resulting from either exceeding a compressive or tensile stress threshold. Simulations including failure criteria were run in Abaqus Explicit 2017 with the same computational resources as the linear simulation. The same boundary conditions were used as in the linear simulation with the following two exceptions. First, the maximum vertical displacement of the top platen was set to $\delta_{max}^{top} =$ 0.055532 mm. This value corresponded to an applied simulation strain (Eq. 2) of $\varepsilon_{app} = 0.6\%$, which was roughly the strain in the experiment at the initial load peak (Fig. 2). Second, the contact between the platens and the specimen was modeled using the general contact formulation in Abaqus[*] rather than using the contact pairs formulation as in the linear simulation. However, the failure simulations used the same normal and tangential interaction properties used in the linear simulation.

The constitutive behavior of the elements was specified using custom-written user-specified material subroutines (VUMAT). For the failure simulations, each of the 101-element sets was assigned a unique material definition including the original density and the two parameters passed to the VUMAT: the Poisson's ratio and $f_{BV,0}$. The Poisson's ratio was set to 0.3 for all elements. The original density (ρ_0, in units of grams per cubic centimeter [g/cm^3]) of each element set was the density of pure bone ($\rho_{b,0}$, for which f_{BV} was 1) scaled by the $f_{BV,0}$ of the elements:

$$\rho_0 = \rho_{b,0} \cdot f_{BV,0} \tag{3}$$

In Eq. 3 the density of pure bone was assumed to be $\rho_{b,0} = 1.8$ g/cm^3 (Mow and Huiskes 2005).

The procedure for calculating the stress for each element at a given increment (timepoint), $t = i$, is detailed in the following and summarized in the flowchart of Fig. 6. Here the current value of variables are referred to with the subscript i, whereas the original value at the start of the simulation (at $t = 0$) are referred to with the subscript 0. All elements were considered active at the start of the simulation ($t = 0$). The current status of the element, "active" or "failed", was tracked through a state-dependent variable, SDV1, as described in Fig. 6.

[*] Described in the online Abaqus Analysis User's Guide, Section 35.4.1: Defining General Contact Interactions in Abaqus/Explicit.

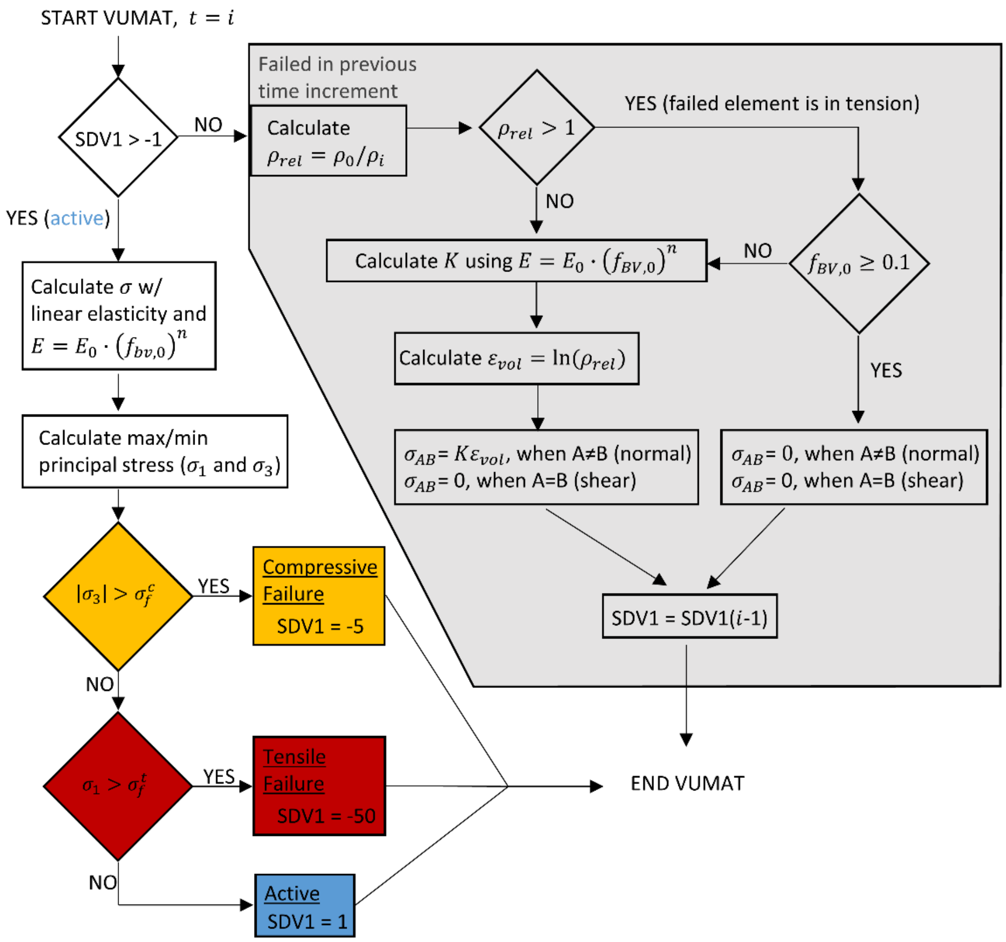

Fig. 6 Conceptual flowchart of VUMAT process for calculating stress and determining the state (active or failed) of each element at a given timepoint, $t = i$

2.4.1 Active Elements

If an element was active (SDV1>–1), the stress of the element was calculated using linear elasticity, with the modulus calculated from $f_{BV,0}$ using Eq. 1. After calculating the stress from the linear elastic equations, the principal stresses of the element were then obtained. The maximum and minimum principal stresses were then compared against failure criteria to determine if the element would fail.

The failure criteria in compression (σ_f^c) and tension (σ_f^t) were calculated for each element from the original bone volume fraction of the element as

$$\sigma_f^c = \sigma_{f,0}^c \cdot (f_{BV,0})^n \tag{4}$$

$$\sigma_f^t = \sigma_{f,0}^t \cdot (f_{BV,0})^k \tag{5}$$

The four parameters governing these criteria were $\sigma_{f,0}^{c}$, $\sigma_{f,0}^{t}$, n, and k, which were iteratively varied to study their effect on the simulation (Appendix B). In the end, to reduce the number of unknown parameters for optimization, the exponents of the power laws were set to n = k = 2 based on reviews of previous experimental studies relating compressive and tensile failure stress to the relative density, which is a correlative measure of BVF (Gibson and Ashby 1997; Morgan et al. 2018). After having specified the exponents to be 2, the remaining parameters were iterated to final values of $\sigma_{f,0}^{c} = \sigma_{f,0}^{t} = 175\ MPa$ to match the experimentally obtained stress–strain beyond the linear region and then the final failure.

The maximum principal stress (σ_1) was compared with the tensile failure stress (Eq. 5), and the element was considered to have failed in tension if

$$\sigma_1 \geq \sigma_f^t \tag{6}$$

Similarly, the minimum principal stress (σ_3) was compared with the compressive failure stress (Eq. 4), and the element was considered to have failed in compression if

$$abs(\sigma_3) \geq \sigma_f^c \tag{7}$$

If the element failed by either compression or tension, the value of the flag noting the state of the element (SDV1) was changed so that the element was considered as "failed" during the next time increment, i+1 (Fig. 6). Once an element had failed, it remained in the failed state until the end of the simulation. If neither Eq. 6 nor Eq. 7 were satisfied, the element was considered to remain active during the next time increment.

2.4.2 Failed Elements

An element was recognized to have already failed in a previous time increment (in either compression or tension) if it had a value of SDV1 < –1 at the start of the VUMAT. In this case the failed element was treated as a fluid for all subsequent time increments: it was nonloadbearing in tension and only carried hydrostatic stress under compression with no shear. For a failed element, first, the relative density of the element, ρ_{rel}, was calculated as the ratio of the original density of the element (Eq. 3) to the current density of the element, ρ_i:

$$\rho_{rel} = \rho_0/\rho_i \tag{8}$$

Equation 8 could be rewritten by using the definition of density as the ratio of mass to volume. Then, with the conservation of mass within each element ($m_i = m_0$), the relative density was expressed as the volume ratio:

$$\rho_{rel} = V_i / V_0 \tag{9}$$

Equation 9 represents the ratio of the current volume of the element at $t = i$, V_i, to the original volume of the element, V_0. Therefore, the relative density provided an indication of whether the element was in a state of tension or compression, and the following check was performed:

$$\rho_{rel} \leq 1 \tag{10}$$

If $V_i < V_0$, Eq. 10 was satisfied, and the failed element was considered to be in compression and to carry stress. In this case the volumetric strain ε_{vol} was calculated as

$$\varepsilon_{vol} = ln(\rho_{rel}) \tag{11}$$

The stress state for the failed element in compression was then calculated from the bulk modulus of the element, K, as

$$\begin{bmatrix} \sigma_{xx} & \sigma_{xy} & \sigma_{xz} \\ \sigma_{xy} & \sigma_{yy} & \sigma_{yz} \\ \sigma_{xz} & \sigma_{yz} & \sigma_{zz} \end{bmatrix} = \begin{bmatrix} K\varepsilon_{vol} & 0 & 0 \\ 0 & K\varepsilon_{vol} & 0 \\ 0 & 0 & K\varepsilon_{vol} \end{bmatrix} \tag{12}$$

In Eq. 12 the bulk modulus (*K*) was calculated from the original elastic modulus of the element (Eq.1) and the Poisson's ratio.

On the other hand, if $V_i > V_0$, Eq. 10 was not satisfied, and the failed element was considered to be in a state of tension. The treatment of these elements depended on the original BVF of the element, $f_{BV,0}$. If $f_{BV,0} \geq 0.1$, the element did not carry any stress for $t = i$. If $f_{BV,0} < 0.1$, the element was treated as if it was in compression, and it carried stress as determined by Eqs. 11 and 12. Treating as loadbearing the low-BVF elements that had previously failed and were subsequently in tension was a numerical approximation employed to mitigate these elements from becoming severely distorted, as described in Appendix C. This approximation did not have a noticeable effect on the stress–strain response (Appendix C).

3. Results

The parameters chosen for the failure limits (Eqs. 4 and 5) were the same between tension and compression. The leading coefficients were set as $\sigma_{f,0}^{c} = \sigma_{f,0}^{t} =$ 175 MPa, and the exponents were $k = n = 2$. Figure 7 compares the stress–strain response of the experiment with the simulation using these failure limits. The compressive strain in the loading direction is also compared between the simulation and the experiment, analogous to Fig. 5, which was for the linear simulation without incorporation of the failure.

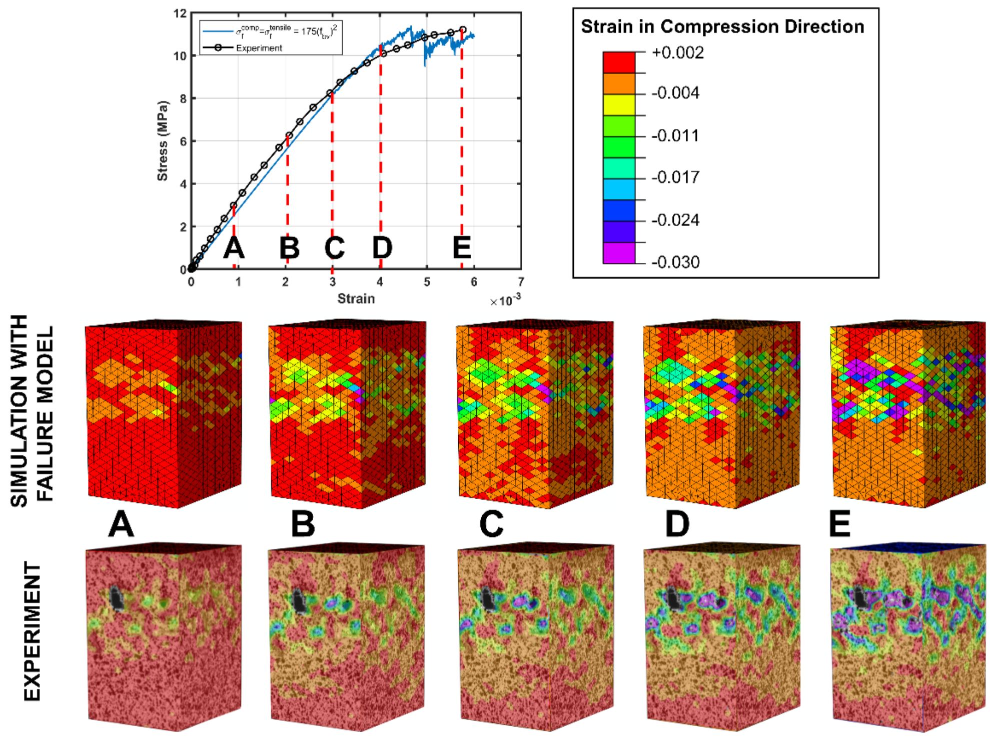

Fig. 7 Comparisons between uniaxial stress–strain response from the simulation with failure and the experiment (top) and for the strain in the loading direction (contours on bottom). The strain values A–D correspond to the same strain values as in Fig. 5 (for the linear simulation without failure).

Figure 8 compares the surface failed elements of the simulation with the experimentally measured principal surface strain fields, which were derived using DIC measurements. Figure 9 compares the timing of element failure with the stress–strain response by showing the $f_{BV,0}$ of each failed element (Fig. 9a) and the total number of failed elements (Fig. 9b) during the simulation. Figure 10 shows the distribution of $f_{BV,0}$, grouped by 5% increments of $f_{BV,0}$. For each group, Fig. 10 indicates the ratio of active elements to failed elements at the end of the simulation. A total of 2595 elements failed in compression (15.6% of the total number of elements in the mesh), while 266 elements (1.6%) failed in tension.

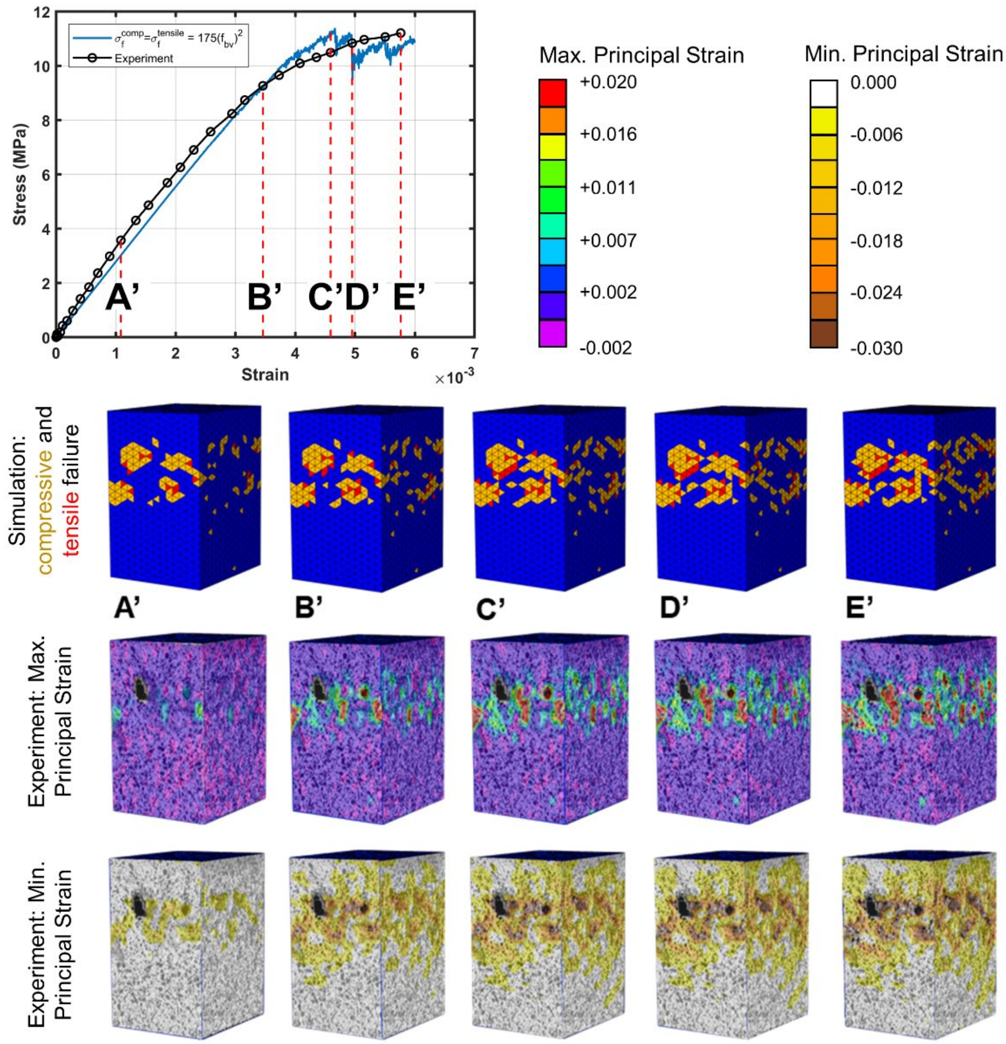

Fig. 8 Comparison of the location of failed elements in the simulation (top row) with the maximum and minimum principal strain fields measured in the experiment (middle row and bottom row, respectively). The simulation and experiment are compared at four different levels of applied strain, labeled as A' through D' and identified on the stress–strain curves at top. At each of the four levels, the sides facing the left and right cameras are shown (identified in Fig. 3). For the simulation images, active elements are shown in blue, elements that previously failed in compression in gold, and elements that previously failed in tension in red. Colors on the experimentally measured strain fields correspond to levels of maximum principal strain as depicted in the color bars at top, where positive and negative values indicate tension and compression, respectively.

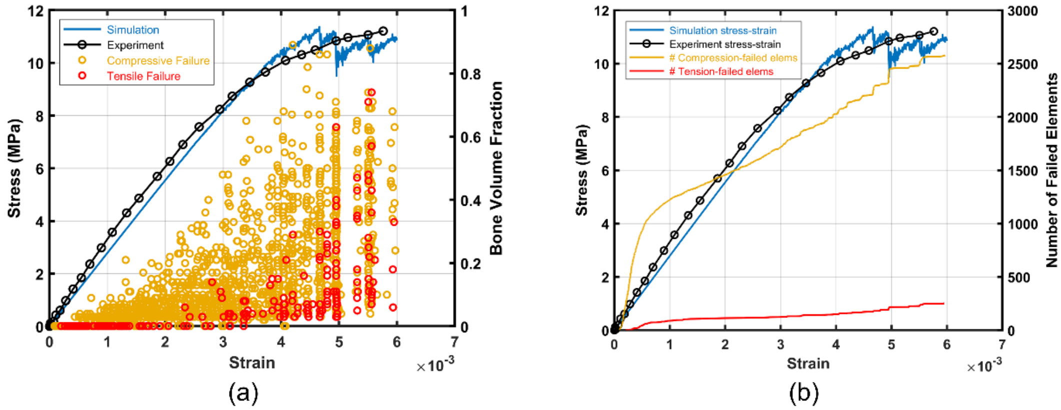

Fig. 9 **Comparison of stress–strain response with timing of element failure. The stress–strain responses from the simulation and experiment are plotted as in Fig. 7. a) Each element failure is depicted with a circle, with a BVF shown by axes on right. b) Cumulative number of elements that failed by each mechanism during the simulation is plotted. In both 9a and 9b, color indicates failure type as in Fig. 8 (gold = compression, red = tension).**

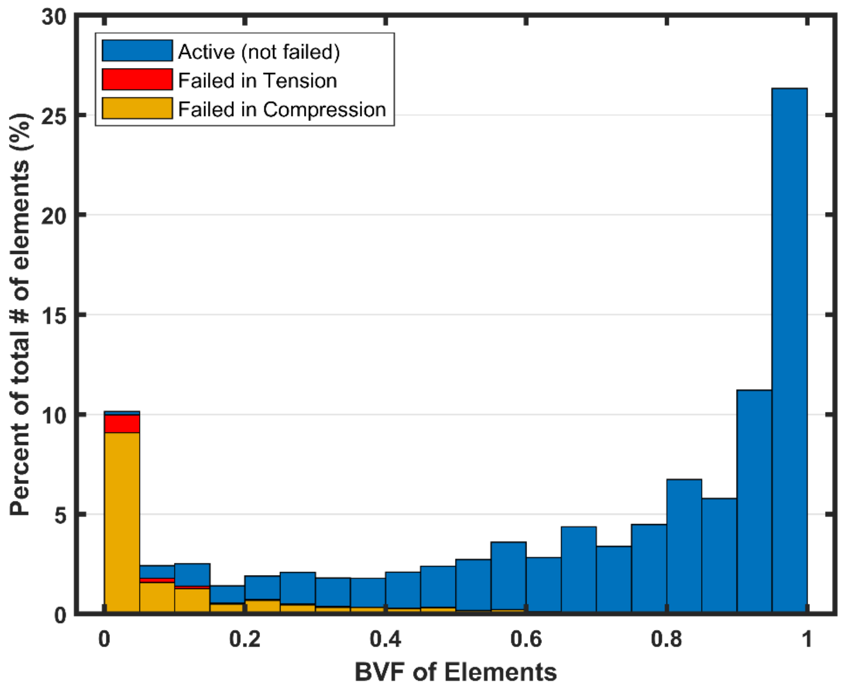

Fig. 10 **Distribution of the original BVF of the elements and the ratio of active to failed elements at the end of the simulation. Elements are grouped into $f_{BV,0}$ increments of 5%. For each group the ratio of active elements at the end of the simulation is shown in blue, elements that failed in tension in red, and compressively failed elements in gold. Total number of elements was 16,683.**

4. Discussion

4.1 Linear Response Modeled Using E–BVF Power Law

The linear portion of the compressive response of skull bone was modeled by assigning element-specific moduli using the ARL power law for the modulus of human skull bone (Eq. 1). The parameters of the E–BVF power law relationship were derived from the experimentally measured *surface* stress–strain by approximating each specimen used in the experimental study as a stack of layers, each layer with uniform properties, and employing the iso-stress assumption: the far-field compressive stress measured by the load cell (at the platen) was assumed to be the same stress acting throughout the structure during the initial linear loading of the compressive response, such that the stress at any given timepoint was invariant with respect to position within the structure. In addition, the strain within a layer, which in reality was heterogeneous, was approximated with a single value calculated from the measured average surface strain of the layer. The present study provided a means of testing these assumptions because the 3-D material heterogeneity was modeled at the length scale of the element. The ability of the linear simulation to match the linear-regime modulus of the experiment to within 5% indicated that these assumptions were sufficient to capture the mesoscale response, providing a less complex method of measuring the strain for researchers in future.

The validity of the modeling procedure used to derive the E–BVF power law was further demonstrated by treating Specimen 04-09, which was simulated here, as a completely separate independent test case. The E–BVF power law given previously as Eq. 1 was originally derived from the data of seven coupons including Specimen 04-09. To treat Specimen 04-09 as a separate test case, the E–BVF power law was recalculated by excluding the data from this specimen and only using the data from the other six specimens. This procedure is detailed in Appendix D, where it is shown that the new, recalculated power law was almost unchanged. In addition, the failure simulation was rerun as described in Section 2.4, with the only difference being that the new, recalculated E–BVF power law was used in place of the relationship given in Eq. 1. However, using these two different power laws did not produce significantly different simulation load-displacement responses (Appendix D).

The applicability of the iso-stress assumption was further investigated by plotting the variation of compressive stress throughout the heterogeneous FE mesh. The minimum principal stress for each element, σ_3, was extracted from the linear simulation at the timepoint marked in Fig. 4 as TimePoint A and are shown in

Fig. 11a. Then the original position of each element in the undeformed mesh was used to calculate the depth of the element such that a depth of 0% corresponded to the bottom of the mesh and a depth of 100% corresponded to the top of the mesh, as annotated in Fig. 11a. Next the depth was divided into 10 levels of 10% each, and the elements were sorted into the levels according to their depth values. The depth was divided into 10 levels to directly compare with the modeling technique previously used to derive the skull bone E–BVF power law (Alexander et al. 2020). Figure 11b plots the mean and standard deviation of σ_3 over each of these 10 levels, where the standard deviation is a measure of the total amount of variation of σ_3 within the x, y, and z dimensions of the level.

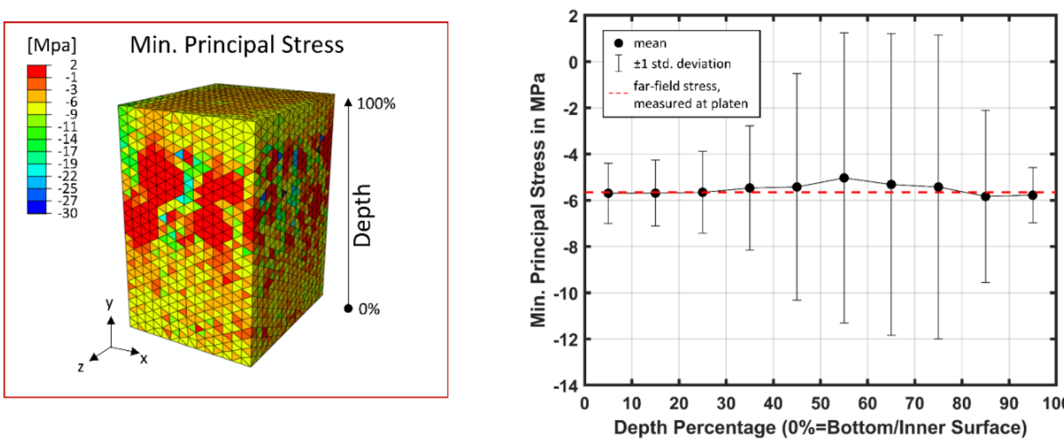

(a) (b)

Fig. 11 Variation of the minimum principal stress (σ_3) in the linear simulation at TimePoint A (marked in Fig. 4). a) Stress values plotted on the undeformed mesh, with depth depicted as varying from 0% at the bottom to 100% at the top. Elements with black color have values of $\sigma_3 < -30$ MPa. b) Depth was divided into 10 groups of depth = 10% each. The mean (filled circle) and standard deviation (error bars) within each group are plotted together with the far-field, apparent stress (red dashed line) calculated from the resultant force on the platen.

As shown in Fig. 11, the stress varied within the layers as expected from the heterogeneity of the material properties within the layer. The greatest variation occurred in the middle layers corresponding to the diploe, likely because there was also greater variation in the BVF in the diploe than in the tables, which were relatively homogenous. Despite these variations, the average within each layer matched the far-field stress to within 1 MPa. An additional insight provided by Fig. 11 is that the specimen had elements with a nonnegative value of σ_3, which indicates that these elements were in tension despite the specimen being loaded in simple compression. This was also likely due to the material heterogeneity and emphasized the importance of including a tensile failure criterion in the failure simulation.

4.2 Failure Criteria Used to Model Secondary Softening

The softening evidenced in the experimental compression curve was modeled through tensile and compressive failure criteria. These criteria were dependent on the BVF by power relationships, Eqs. 4 and 5. The exponents of the power law were chosen as $k = n = 2$. The leading coefficients, $\sigma^t_{f,0}$ and $\sigma^c_{f,0}$, represented the compressive and tensile strength of pure bone tissue (BVF = 1), and the final values after iterating were $\sigma^t_{f,0} = \sigma^c_{f,0} = 175$ MPa. There are many factors to consider when comparing the leading coefficients of the power law and nonporous bone tissue strength with literature values. First, the skull bone coupon modeled in the present study consisted of all three layers of the skull sandwich structure, including not only cortical, but also trabecular bone. Therefore, deriving a single power relationship between the failure strength and the BVF for the skull bone assumed that the bone tissue/material (BVF = 1) in trabecular bone had the same mechanical properties as bone tissue in the cortical bone. However, Gibson and Ashby (1997), in reviewing the pertinent literature at the time, noted that there had not been direct experiments performed to measure the strength of trabecular bone material. They therefore calculated the compressive and tensile strength of trabecular bone tissue to be 136 and 105 MPa, respectively, by scaling down the corresponding strengths of cortical bone tissue by 70%. Similarly, Bayraktar et al. (2004) found the compressive and tensile strength of trabecular bone tissue in the human femur to be on average 137 and 83 MPa, respectively, which were approximately 20%–30% less than the corresponding strengths of cortical bone tissue.

Second, the majority of studies, which related the mechanical properties of bone to the BVF, were performed on bone samples originating from anatomical locations other than the skull. However, power relationships between BVF and mechanical properties likely change based on the anatomical sites from which the bones were extracted, as demonstrated by Morgan et al. (2003) for the case of modulus–density relationships. A power-law relationship specifically for human skull in tension was published by Boruah et al. (2017). The tensile failure stress was related to the BVF of the outer cortical layer as $\sigma^t_f = 109.54\left(f_{BV,0}\right)^{2.79}$ MPa. However, the BVF under consideration was only on a small range, roughly 60%–90%, having used only specimens from the outer cortical table.

Given the previously mentioned caveats and considerations, a few comparisons with previous literature can be drawn for the compressive and tensile failure criteria of Eqs. 4 and 5. First, the dependence of the tensile and compressive strengths on the square of the BVF matches previous experimental results, as described in the reviews by Gibson and Ashby (1997) and Morgan et al. (2018). Second, using the same value of failure strength for both tensile and compressive failure deviates from previous studies that indicated that bone is stronger in compression than in tension (Gibson and Ashby 1997; Bayraktar et al. 2004; Morgan et al. 2018). Third, the value of the tissue compressive and tensile strength of 175 MPa is higher than the results summarized previously. Possible explanations for these differences are the assumptions and limitations of the current study, as in the following.

4.3 Critical Assumptions and Limitations

The failure simulations were carried out in Abaqus Explicit owing to problems with convergence encountered during preliminary simulations attempted in Abaqus Standard. In the experiment the compression was applied at a quasi-static nominal strain rate of 0.001/s (Alexander et al. 2020). However, in the failure simulations the platen was specified to move at a speed of approximately 11.1 mm/s, thereby applying a nominal strain rate of 1.2/s. This non-quasi-static speed was chosen to reduce the computation time of the explicit solver to complete the simulation within a few hours. To assess whether the simulation could still be approximated as quasi-static, the kinetic energy (KE) and internal energy (IE) were output during the simulation, and the percentage of KE to IE was calculated. The KE/IE percentage never exceeded 2%, with an average of <0.1%. Explicit simulations of quasi-static experiments are recommended to stay within a KE/IE percentage of 5% (Gulavani et al. 2014). Others have used this 5% bound as a criterion of ensuring that kinetic energy is not dominating the response (e.g., Kader et al. 2017; Kandail et al. 2018).

The methodology of modeling failure was developed and demonstrated using one specimen by comparing the simulated response with detailed experimental measurements of the response from that specimen. Furthermore, this particular specimen had a nonrectangular shape, due to the difficulty of machining such small specimens from relatively thin skull with a highly porous layer in the middle, as shown in the "Full Specimen" micro-CT images of Fig. 3. The FE mesh was based only on a cut-out of the specimen in the shape of a rectangular parallelepiped ("Rectangular VOI", Fig. 2) in order to use the in-house mapping algorithm.

In the present study the mechanical response of the elements after failure was modeled using an approximate, nonphysical method. For example, if an element was further compressed after failure, it was assumed to only have a volumetric hydrostatic response with no shear resistance with a bulk modulus calculated using the original BVF of the element ($f_{BV,0}$). However, the current BVF of a failed element is expected to be different than the original BVF of the element. Future efforts could attempt to base the postfailure response on the current BVF of the element rather than $f_{BV,0}$.

In the mapping algorithm used here, each voxel in the micro-CT dataset was assigned to a specific element. Therefore, the biofidelity of the mesh may be governed by at least three factors: 1) the size of the elements relative to the size of the voxels, 2) the resolution of the micro-CT scan (the physical volume of bone that each voxel represents), and 3) the relative size of the microstructural features in the specimen that must be captured in the FE mesh. The relative size of the elements to the voxels was quantified by recording the total number of voxels, n_{vox}, assigned to each element when mapping the mesh to the micro-CT data to calculate the $f_{BV,0}$ for each element (Section 2.2). Since each voxel contains information averaged in 3-D, the value of n_{vox} corresponds to the physical volume within the bone specimen the element represented. The frequency distribution of n_{vox} is shown in Fig. 12. This distribution may be favorable for the following reasons. The minimum value of n_{vox} is shown to be greater than 5 voxels. This indicates that the $f_{BV,0}$ value for even the smallest elements was calculated by averaging over more than 5 voxels. If the elements had been too small compared with the voxels, the BVF of the elements would be based on only a few voxels. In this case the model would be susceptible to severe discontinuities in the material properties. Moreover, the average of n_{vox} was between 20 and 40 pixels. If the elements were too large compared with the voxels, the BVF of large elements would be calculated from too many voxels, and the structural variation of the bone specimen would be averaged out.

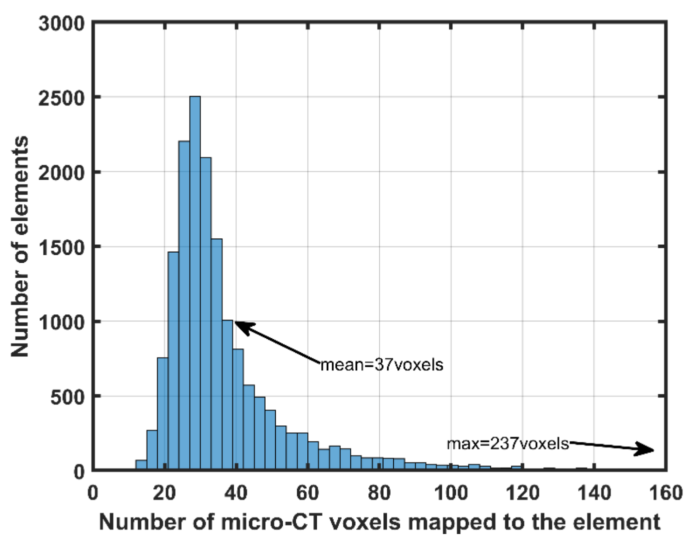

Fig. 12 Frequency distribution of the number of micro-CT voxels (n_{vox}) mapped to each element during the algorithm used to calculate the BVF of each element. The distribution was skewed to the right, with groups of only a few elements having $n_{vox} > 160$.

To compare the size of the elements to the microstructural features, the diameter of the inscribed sphere $d_{inscribed}$ of each element was calculated (Fig. 13a). The value of $d_{inscribed}$ provided an indication of the lengthscale of physical features within the bone coupon that could be completely contained within a single element. The frequency distribution of $d_{inscribed}$ is compared with microstructural features of the bone coupon in Fig. 13.

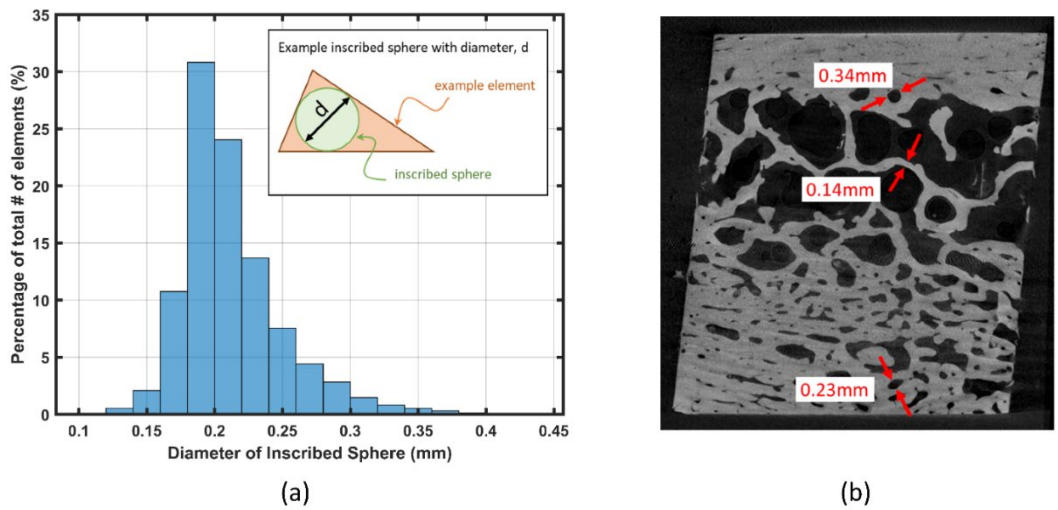

Fig. 13 Size of the elements relative to the microstructural features of the bone specimen. a) Frequency distribution of the diameter of the inscribed sphere of each element. b) Micro-CT image of the face of the specimen imaged by the right camera (shown in Fig. 3, top row). Lengthscale of several features is indicated as a means of comparison with 13a.

5. Conclusions and Future Work

The HEMC mesoscale simulation method involved filling the volume of the specimen with elements and then obtaining the BVF of each element. Next, element-specific material properties were assigned using the E–BVF power law previously optimized for human skull (Alexander et al. 2020). This power relationship was derived with the critical assumption that the skull specimen can be approximated with a stack of microstructurally differing layers but with each layer having different properties that were uniform within the layer. The computational concept developed here for the heterogeneous specimen was able to model the linear portion of the stress–strain response of the coupon with a stiffness deviating by less than 5% from that which was measured experimentally, thus also verifying the use of critical assumptions while experimentally obtaining the E–BVF power-law relationship.

Incorporating and optimizing compressive and tensile power-law failure criteria (Eqs. 4 and 5) enabled the simulation to approximate the subsequent progress of nonlinearity in the experimental stress–strain response and capture the experimentally observed initiation of the final catastrophic failure. The methodology developed to represent the failure initiation enabled the identification of the localized failure instability locations, which were comparable to what was experimentally measured within the skull bone during uniaxial compressive loading, thus validating the extension of the HEMC procedure to the initiation of failure. The ability to predict failure initiation and to identify localized failure locations at coupon scale can be used in future studies to develop simpler approaches for injury biomechanics when focusing on skull fracture at larger scale. Thus, future work will be directed at incorporating the methodology developed here into simulations of skull bone specimen macro-structures with layering to develop simplified predictive capability to be used at larger scale.

6. References

Alexander SL. Gunnarsson CA, Rafael K, Weerasooriya T. Microstructural dependence of the compressive mechanical response of human skull. Aberdeen Proving Ground (MD): Army Research Laboratory (US); 2018 Sep. Report No.: ARL-TR-8512.

Alexander SL, Gunnarsson CA, Weerasooriya T. Influence of the mesostructure on the compressive mechanical response of adolescent porcine cranial bone. Journal of the Mechanical Behavior of Biomedical Materials. 2019a;96:96–107.

Alexander SL, Gunnarsson CA, Weerasooriya T. The compressive mechanical response of the human skull: implementation of morphology-based mechanical deformation model in a 3-D finite-element simulation. Aberdeen Proving Ground (MD): CCDC Army Research Laboratory (US); 2019b Mar. Report No.: ARL-TR-8675.

Alexander SL, Rafaels K, Gunnarsson CA, Weerasooriya T. Structural analysis of the frontal and parietal bones of the human skull. Journal of the Mechanical Behavior of Biomedical Materials. 2019c;90:689–701.

Alexander SL, Gunnarsson CA, Rafaels K, Weerasooriya T. Multiscale response of the human skull to quasi-static compression. Journal of the Mechanical Behavior of Biomedical Materials. 2020;102.

Ariza O, Gilchrist S, Widmer RP, Guy P, Ferguson SJ, Cripton PA, Helgason B. Comparison of explicit finite element and mechanical simulation of the proximal femur during dynamic drop-tower testing. Journal of Biomechanics. 2015;48(2):224–232.

Bayraktar HH, Morgan EF, Niebur GL, Morris GE, Wong EK, Keaveny TM. Comparison of the elastic and yield properties of human femoral trabecular and cortical bone tissue. Journal of Biomechanics. 2004;37(1):27–35.

Bessho M, Ohnishi I, Matsuyama J, Matsumoto T, Imai K, Nakamura K. Prediction of strength and strain of the proximal femur by a CT-based finite element method. Journal of Biomechanics. 2007;40(8):1745–1753.

Boruah S, Henderson K, Subit D, Salzar R, Shender B, Paskoff G. Response of human skull bone to dynamic compressive loading. Proceedings of the International Research Council on Biomechanics of Injury (IRCOBI) Conference; 2013 Sep 11–13; Gothenburg, Sweden. Vol. 13. p. 497.

Boruah S, Subit DL, Paskoff GR, Shender BS, Crandall JR, Salzar RS. Influence of bone microstructure on the mechanical properties of skull cortical bone—a combined experimental and computational approach. Journal of the Mechanical Behavior of Biomedical Materials. 2017;65:688–704.

Gibson LJ, Ashby MF. Cellular solids: structure and properties. Cambridge (UK): Cambridge University Press; 1997.

Gulavani O, Hughes K, Vignjevic R. Explicit dynamic formulation to demonstrate compliance against quasi-static aircraft seat certification loads (CS25. 561). Part I: influence of time and mass scaling. Proceedings of the Institution of Mechanical Engineers, Part G: Journal of Aerospace Engineering. 2014;228(11):1982–1995.

Hambli R. Micro-CT finite element model and experimental validation of trabecular bone damage and fracture. Bone. 2013;56(2):363–374.

Helgason B, Perilli E, Schileo E, Taddei F, Brynjólfsson S, Viceconti M. Mathematical relationships between bone density and mechanical properties: a literature review. Clinical Biomechanics. 2008;23(2):135–146.

Kader MA, Islam MA, Saadatfar M, Hazell PJ, Brown AD, Ahmed S, Escobedo JP. Macro and micro collapse mechanisms of closed-cell aluminum foams during quasi-static compression. Materials & Design. 2017;118:11–21.

Kandail HS, Trivedi SD, Shaikh AC, Bajwa TK, Daniel PO, Jahangir A, LaDisa Jr JF. Impact of annular and supra-annular CoreValve deployment locations on aortic and coronary artery hemodynamics. Journal of the Mechanical Behavior of Biomedical Materials. 2018;86:131–142.

Morgan EF, Bayraktar HH, Keaveny TM. Trabecular bone modulus density relationships depend on anatomic site. Journal of Biomechanics. 2003;36(7):897–904.

Morgan EF, Unnikrisnan GU, Hussein AI. Bone mechanical properties in healthy and diseased states. Annual Review of Biomedical Engineering. 2018;20:119–143.

Mow VC, Huiskes R. Basic orthopaedic biomechanics and mechano-biology. 3rd ed. Baltimore (MD): Lippincott Williams and Wilkins; 2005.

Musy SN, Maquer G, Panyasantisuk J, Wandel J, Zysset PK. Not only stiffness, but also yield strength of the trabecular structure determined by non-linear μFE is best predicted by bone volume fraction and fabric tensor. Journal of the Mechanical Behavior of Biomedical Materials. 2017;65:808–813.

Robbins DH, Wood JL. Determination of mechanical properties of the bones of the skull. Experimental Mechanics. 1969;9(5):236–240.

Appendix A. Effect of Platen/Specimen Friction Coefficient

A tangential friction coefficient of $\mu = 0.1$ between the specimen and the platens was used for both simulations: the simulation that only modeled the linear regime as well as for the simulation that included nonlinear deformation and failure. The effect of the magnitude of this friction coefficient parameter was tested by running an additional linear simulation using the same setup as described in the main body of the report (Section 2.3) but with a tangential friction coefficient reduced by an order of magnitude to $\mu = 0.01$. The apparent stress–strain curve, analogous to Fig. 4 of the main report, is shown in Fig. A-1. Reducing μ by an order of magnitude was seen to be negligible with a reduction in modulus of less than 1%. It was therefore concluded that the friction coefficient between the specimen and the platens was not a governing parameter in the simulations.

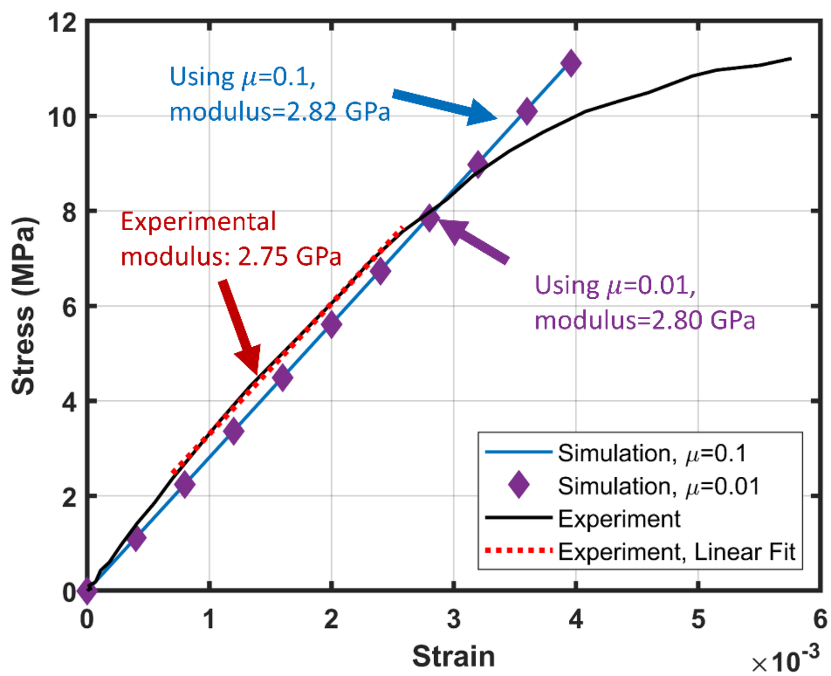

Fig. A-1 Effect on the apparent stress–strain response of reducing the friction coefficient between the platens and the specimen by an order of magnitude

Appendix B. Representative Effect of Failure Strength Parameters

In the failure simulation of this study, compressive and failure strengths (σ_f^c and σ_f^t, respectively) were calculated for each element using power laws based on the initial bone volume fraction (BVF) of the element, $f_{BV,0}$ (Eqs. 4 and 5 of the main report). Each power law consisted of a leading coefficient and an exponent that scaled $f_{BV,0}$. The effects of the leading coefficient and the exponent on the stress–strain response are demonstrated in Figs. B-1 and B-2, respectively. These show the stress–strain response of failure simulations identical to that of the main body of the report, apart from the parameters of the power laws used to calculate the failure stresses. Only a few representative simulations are included here to provide a general idea of the parameter effects. The total number of simulations used to iteratively identify the parameters was many more than included here.

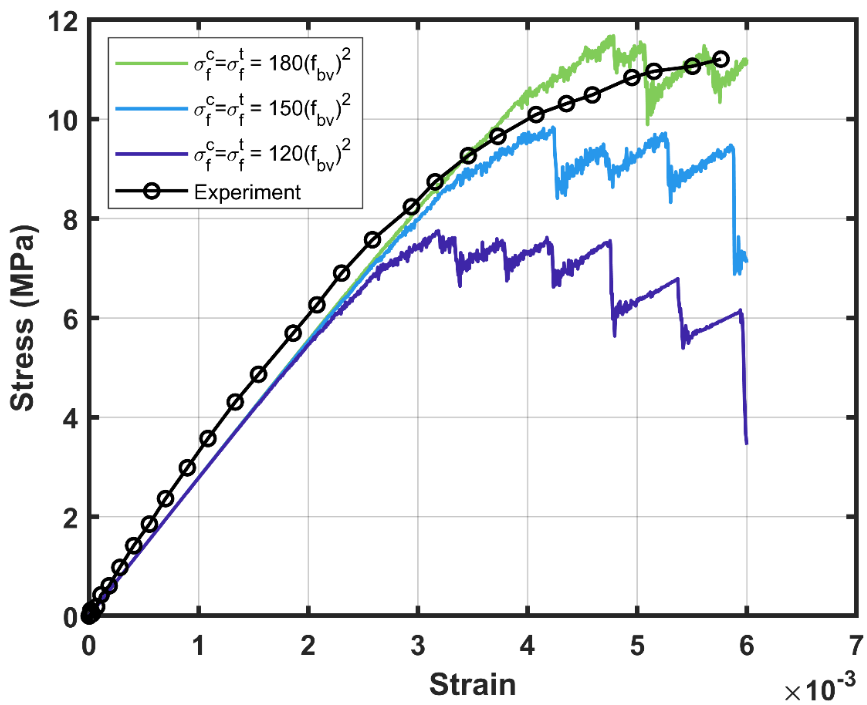

Fig. B-1 Effect of scaling the leading coefficient of the failure stress power laws

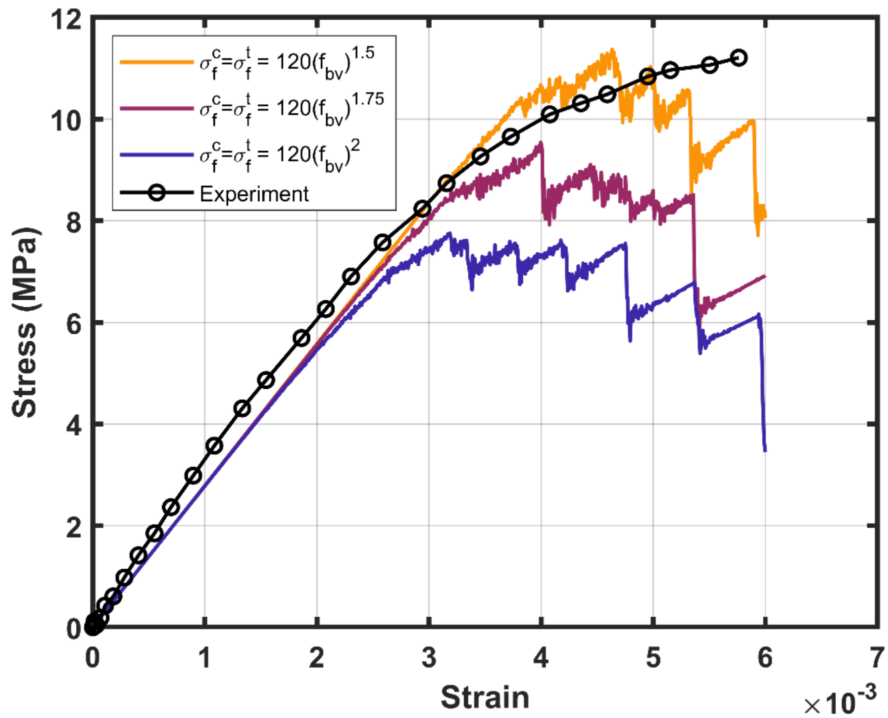

Fig. B-2 Effect of scaling the exponents of the failure stress power laws. All three simulations used identical leading coefficients of 120 MPa. Simulation using $\boldsymbol{\sigma_f^c = \sigma_f^t = 120 \cdot \left(f_{BV}\right)^2}$ was also plotted in Fig. B-1.

Appendix C. Effect of Low-Bone Volume Fraction (BVF) Elements Carrying a Tensile Stress after Failure

Once an element had failed in the failure simulation, in subsequent timesteps, the VUMAT checked whether the failed element was in a state of tension or compression (Section 2.4.2 of the main report). This was determined by calculating the relative density, which was equivalent to the ratio of the current volume of the element V_i to the original volume of the element V_0 (Eqs. 8 and 9 of the main report). If $V_i > V_0$, the failed element was considered as being in a state of tension.

Physically, failed elements loaded in tension should not carry stress. However, in the failure simulations described in this report, an approximation was employed to avoid the failed elements from becoming overly distorted. This approximation is hereafter referred to as the restorative-force approximation (RFA), and it consisted of considering failed elements as load bearing if the original BVF of the element, $f_{BV,0}$, was less than 10% (Section 2.4.2 of the main report). The effect of the RFA was tested by comparing two preliminary simulations. These preliminary simulations were identical to the failure simulation of the main body of this report, except that they used a different modulus (E)–BVF power law [$E = 8.755\left(f_{BV,0}\right)^{1.603}$] and one of them lacked the RFA. In the simulation without the RFA, all elements that had previously failed and were subsequently in a state of tension were considered nonloadbearing regardless of $f_{BV,0}$. Figure C-1 provides a flowchart highlighting the effect of excluding the RFA on the VUMAT algorithm for determining the stress of failed elements.

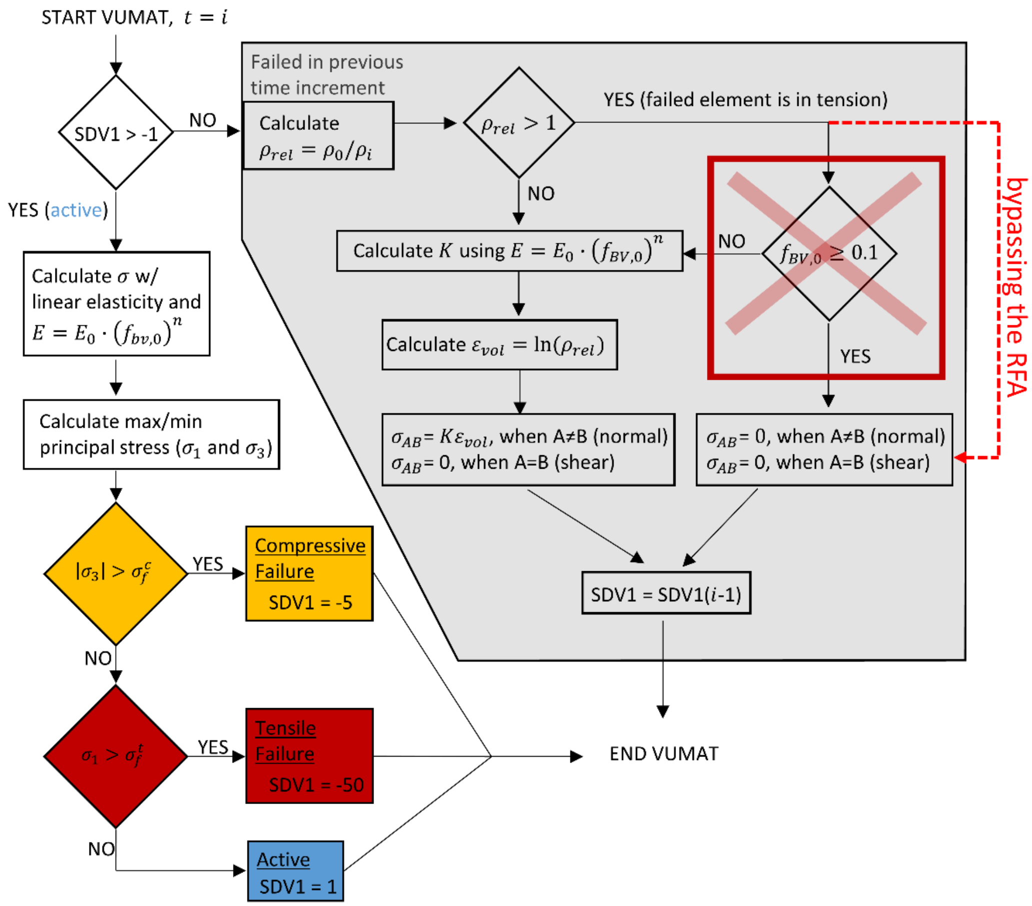

Fig. C-1 VUMAT flowchart showing the calculation of stress in preliminary simulations run without using the restorative-force approximation. The VUMAT is identical to that presented in the main body of the report (Fig. 6) except that the procedure for the restorative-force approximation is bypassed (box with red X). Therefore, all previously failed elements with $\boldsymbol{\rho_{rel} > 1}$ were set to be nonloadbearing (red dotted line).

Figure C-2 compares the effective stress–strain curves for simulations with and without the RFA, together with the final shape of the deformed mesh after compression. The effect of the RFA is shown in comparing the deformed meshes. In both cases, some elements with very low BVF values became severely distorted after having failed during the simulation. However, the number of distorted elements, and the extent of the distortion, is limited by the RFA. At the same time, it is shown that this approximation only negligibly affects the stress–strain response; the stress–strain curves are indistinguishable in the linear regime and only slightly deviate thereafter. Therefore the RFA was used in the failure simulations of the report due to the highly advantageous effect on element distortion and negligible effect on the stress–strain response.

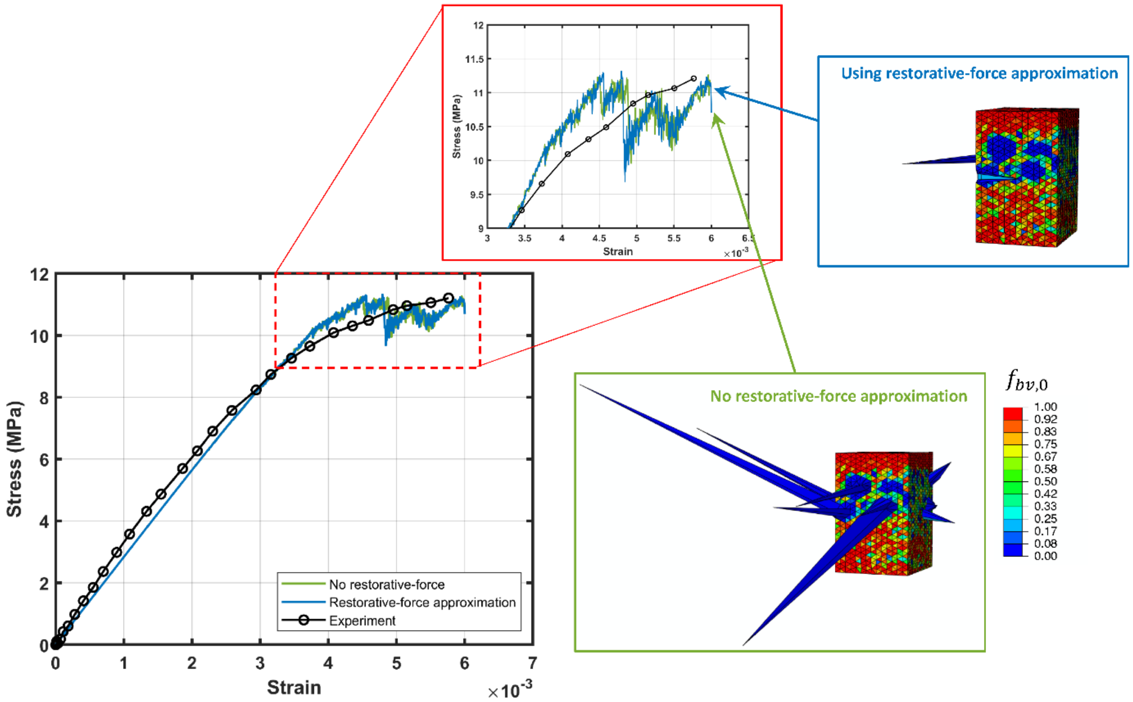

Fig. C-2 Effect of the restorative-force approximation on the stress–strain response and on element distortions. The deformed meshes at the end of the simulations with and without the approximation are shown on the upper and lower right, respectively. Contours show the original BVF of the elements (both meshes use the same color map).

Appendix D. Considering Specimen 04-09 as a Completely Separate Test Case

D.1 Introduction

In the simulation as described in Section 2.4 of the main report, the modulus (E) was calculated using the modulus–bone volume fraction (E–BVF) power law reported in Alexander et al.[1]:

$$E = 8.528\left(f_{BV,0}\right)^{1.585} \quad \text{(D-1)}$$

The power law of Eq. D-1 had been calculated from experiments on seven coupons, including Specimen 04-09. Specimen 04-09 was simulated in the present study.

In this appendix the modeling procedure was essentially repeated de novo so as to treat Specimen 04-09 as a completely new specimen and a completely separate experiment. To accomplish this, the E–BVF power relationship was recalculated without Specimen 04-09. This new relationship, calculated from the other specimens, was then applied to simulate the compression experiment of Specimen 04-09. The stress–strain response was compared between the simulation and experiment to confirm the validity of the modeling procedure by treating Specimen 04-09 as a confirmation test case.

D.2 Methods and Results

First, the E–BVF power law was recalculated **without** using the data from Specimen 04-09. Instead, only the data from the other six specimens of Alexander et al.[1] were included. The resulting power law was

$$E = 8.658\left(f_{BV,0}\right)^{1.600} \quad \text{(D-2)}$$

Figure D-1 compares these two power law fits.

[1] Alexander SL, Gunnarsson CA, Rafaels K, Weerasooriya T. Multiscale response of the human skull to quasi-static compression. Journal of the Mechanical Behavior of Biomedical Materials. 2020;102.

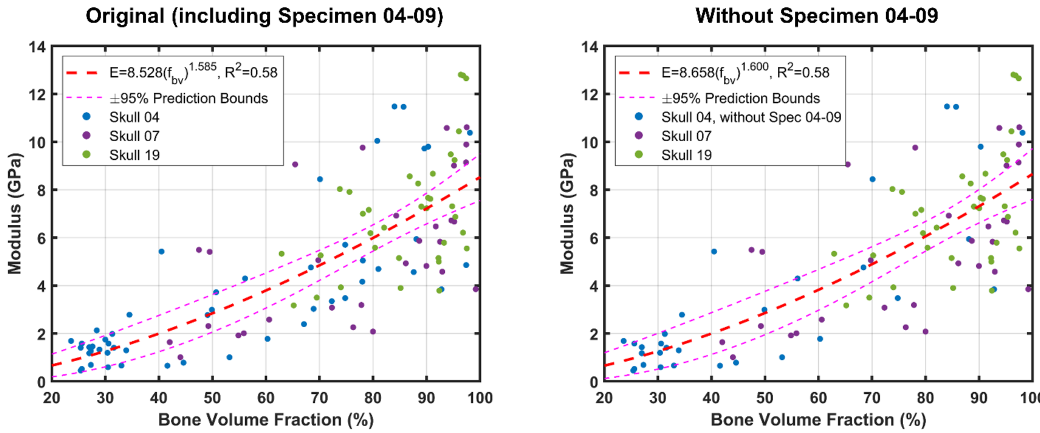

Fig. D-1 Effect of removing Specimen 04-09 on the E–BVF power relationship. (left) Original power relationship calculated with Specimen 04-09 included.[1] Seven coupons were used: three from Skull 04, two from Skull 07, and two from Skull 19. (right) Power relationship recalculated after removing the data from Specimen 04-09. Thus, the data were from a total of six coupons.

Next the simulation of Specimen 04-09 was run following exactly the procedures outlined in Section 2.4 of the main report with the exception that the E–BVF power law was changed to Eq. D-2. This simulation is referred to as the "Excluded-Simulation" since the E–BVF relationship was calculated without Specimen 04-09. In contrast, the original simulation, which used Eq. D-1, is referred to as the "Included-Simulation" since Specimen 04-09 was included in the E–BVF power law calculation. Figure D-2 compares the stress–strain response for the Excluded-Simulation and Included-Simulation.

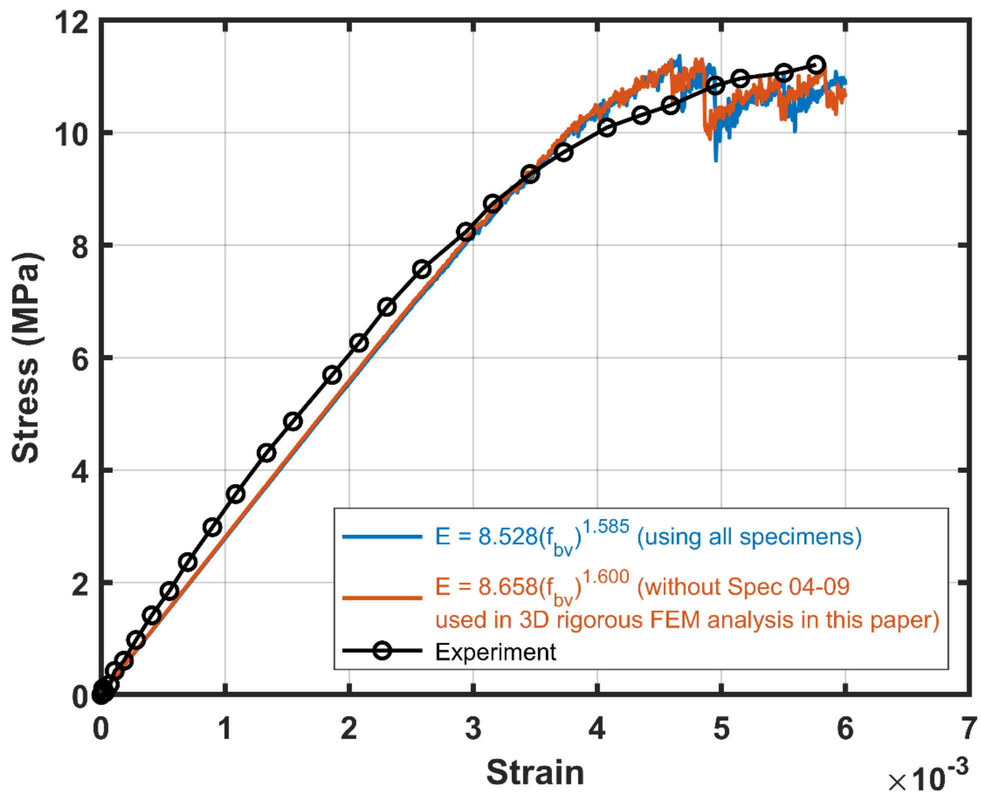

Fig. D-2 Stress–strain response of Specimen 04-09 comparing the Included-Simulation and the Excluded-Simulation. The Included-Simulation (blue curve) used the E–BVF power relationship from Alexander et al. 2020 (Eq. D-1), which was calculated with the data from Specimen 04-09 included. The Excluded-Simulation (orange curve) used an E–BVF power relationship recalculated after excluding the data from Specimen 04-09 (Eq. D-2).

D.3 Conclusion

In this appendix Specimen 04-09 was treated as a completely separate specimen from the original experimental cohort of Alexander et al.[2] Removing the data from Specimen 04-09 caused only a minor change in the E–BVF power relationship because there were still the data from the six other coupons. Furthermore, using the updated E–BVF power relationship to simulate the compression of Specimen 04-09 did not significantly alter the stress–strain response compared with the original Included-Simulation. These findings confirm the validity of the modeling procedure described in Section 2.4 of the main report, as well as the validity of the derived power laws.

[2] Alexander SL. Gunnarsson CA, Rafael K, Weerasooriya T. Microstructural dependence of the compressive mechanical response of human skull. Aberdeen Proving Ground (MD): Army Research Laboratory (US); 2018 Sep. Report No.: ARL-TR-8512.

List of Symbols, Abbreviations, and Acronyms

2-D	two-dimensional
3-D	three-dimensional
ARL	Army Research Laboratory
BVF	bone volume fraction
CCDC	US Army Combat Capabilities Development Command
DIC	digital image correlation
E	modulus
E–BVF	modulus–bone volume fraction
FE	finite element
g/cm^3	grams per cubic centimeter
GPa	gigapascal
HEMC	hybrid experimental–modeling–computational
IE	internal energy
K	bulk modulus
KE	kinetic energy
μ-CT	micro-computed tomography
RFA	restorative-force approximation
VOI	volume of interest

1 (PDF) DEFENSE TECHNICAL INFORMATION CTR
DTIC OCA

1 (PDF) CCDC ARL
FCDD RLD CL
TECH LIB

11 (PDF) CCDC NATICK SOLDIER SYSTEMS CTR
M G CARBONI
D COLANTO
R DILLALLA
B FASEL
J FONTECCHIO
B KIMBALL
J KIREJCZYK
J PARKER
M MAFEO
M MARKEY
D PHELPS

3 (PDF) PROG EXECUTIVE OFC SOLDIER
J HOPPING
J MULLENIX
D OTTERSON

1 (PDF) US ARMY TEST AND EVALUATION COMMAND
A FOURNIER

1 (PDF) MTRL SCIENCES DIV
LAWRENCE BERKELY NATL LAB
R RITCHIE

1 (PDF) SOUTHWEST RSRCH INST
C ANDERSON JR
S CHOCRON
D NICOLELLA
T HOLMQUIST
G JOHNSON

1 (PDF) NIST
M VANLANDINGHAM

1 (PDF) INST FOR DEFNS ANLYS
Y MACHERET

1 (PDF) CO-AUTHOR
B SCOTT

3 (PDF) MRMC DOD BLAST INJURY RSRCH PROGRAM COOR OFC
R GUPTA
T PIEHLER
R SHOGE

2 (PDF) MRMC JTAPIC PRGM OFC
W LEI
J USCILOWICZ

1 (PDF) WIAMAN PMO
K LOFTIS

4 (PDF) US ARMY AEROMEDICAL RSRCH LAB
F BROZOSKI
V CHANCEY
B MCENTYRE
D WISE

1 (PDF) CCDC GROUND VEHICLE SYSTEMS CENTER
R SCHERER

1 (PDF) CCDC
AMSRD PE
D RUSIN

2 (PDF) CCDC CHEMICAL BIOLOGICAL CENTER
M HORSMON
N VINCELLI

1 (PDF) OSD DOT&E
J IVANCIK

5 (PDF) US NAVAL RESEARCH LABORATORY
A BAGCHI
A ILIOPOULOS
J MICHOPOULOS
K TEFERRA
X TAN

4 (PDF) CCDC DAC
FCDD DAS LBW
G DIETRICH
FCDD DAS LBE
J GURGANUS
W MERMAGEN
S SNEAD

86 (PDF) CCDC ARL
FCDD RLR
D STEPP
FCDD RLW
S WALSH
S KARNA
A RAWLETT
S SCHOENFELD
J ZABINSKI
FCDD RLW P
R FRANCART
FCDD RLW L
T V SHEPPARD
A DAGRO
C GOOD
FCDD RLW M
B CHEESEMAN
E CHIN
J LA SCALA
FCDD RLW B
R BECKER
J CAMPBELL
P GILLICH
C HOPPEL
B SCHUSTER
A TONGE
L VARGAS-GONZALEZ
FCDD RLW LF
G BROWN
FCDD RLW LH
T EHLERS
J BEATTY
L MAGNESS
C MEYER
J NEWILL
D SCHEFFLER
FCDD RLW MA
T BOGETTI
T PLAISTED
J SANDS
E WETZEL
C YEN
FCDD RLW MB
D O’BRIEN
G GAZONAS
B LOVE
P MOY
J SIETINS
J SUN
T WALTER
FCDD RLW MC
R JENSEN
FCDD RLW MD
A BUJANDA
K CHO
FCDD RLW ME
J LASALVIA
P PATEL
S SILTON
J SWAB
FCDD RLW MF
K DARLING
B DOWDING
S GRENDAHL
H MURDOCH
FCDD RLW MG
J ANDZELM
J LENHART
R MROZEK
FCDD RLW PA
S BILYK
FCDD RLW PB
S ALEXANDER
T BAUMER
A BROWN
B FAGAN
A GOERTZ
A GUNNARSSON
C HAMPTON
M KLEINBERGER
E MATHEIS
J MCDONALD
P MCKEE
K RAFAELS
S SATAPATHY
M TEGTMEYER
T WEERASOORIYA
S WOZNIAK
T ZHANG
FCDD RLW PC
J CAZAMIAS
D CASEM
J CLAYTON
C MEREDITH
L SHANNAHAN
J LLOYD
FCDD RLW PD
K MASSER
R DONEY
C RANDOW
FCDD RLW PE
M LOVE
P SWOBODA
FCDD RLW PG
N GNIAZDOWSKI
R GUPTA
S KUKUCK

4 (PDF) WHITING SCHOOL OF ENG
JOHNS HOPKINS UNIV
KT RAMESH
T D NGUYEN
B NOTGHI
S BAILOOR

2 (PDF) COULTER DEPT OF BIOMED ENG
GEORGIA INST OF TECH
S MARGULIES
D MCDOWELL

1 (PDF) DEPT OF ENGRNG SCI AND MECHANICS
VIRGINIA POLYTECHNIC INST AND STATE UNIV
R BATRA

3 (PDF) MASSACHUSETTS INST OF TECHLGY
INST FOR SOLDIER NANOTECHNOLOGIES
R RADOVITZKY
S SOCRATE
M J BUEHLER

1 (PDF) DEPT OF MECHL AND NUCLEAR ENGRNG
THE PENNSYLVANIA STATE UNIV
R KRAFT

1 (PDF) INDIAN INST OF TECH
R BHARDWAJ

2 (PDF) CENTER FOR APPLIED BIOMECHANICS
UNIV OF VIRGINIA
R SALZAR
M B PANZER

1 (PDF) UCSD MAT SCI AND ENG
MARC MEYERS

1 (PDF) DUKE UNIV
BIOMED ENG
CR BASS

1 (PDF) UNIV OF CAPE TOWN
BLAST IMPACT & SURVIVABILITY UNIT
TJ CLOETE

1 (PDF) UNIV OF OXFORD
BLAST IMPACT & SURVIVABILITY UNIT
C SIVIOUR

1 (PDF) UNIV OF CAMBRIDGE
ENG DEPT
V DESHPANDE

2 (PDF) UNIV OF SOUTH CAROLINA
COL OF ENG
M SUTTON
S SOCKALINGAM